mathematics

MDPI

Article

AFSA-FastICA-CEEMD Rolling Bearing Fault Diagnosis Method Based on Acoustic Signals

Jin Yan [1,2], Fubing Zhou [1], Xu Zhu [1] and Dapeng Zhang [1,2,*]

[1] Guangdong Provincial Key Laboratory of Intelligent Equipment for South China Sea Marine Ranching, Guangdong Ocean University, Zhanjiang 524088, China
[2] Shenzhen Research Institute, Guangdong Ocean University, Shenzhen 518120, China
* Correspondence: zhangdapeng@gdou.edu.cn

Abstract: As one of the key components in rotating machinery, rolling bearings have a crucial impact on the safety and efficiency of production. Acoustic signal is a commonly used method in the field of mechanical fault diagnosis, but an overlapping phenomenon occurs very easily, which affects the diagnostic accuracy. Therefore, effective blind source separation and noise reduction of the acoustic signals generated between different devices is the key to bearing fault diagnosis using acoustic signals. To this end, this paper proposes a blind source separation method based on an AFSA-FastICA (Artificial Fish Swarm Algorithm, AFSA). Firstly, the foraging and clustering characteristics of the AFSA algorithm are utilized to perform global optimization on the aliasing matrix W, and then inverse transformation is performed on the global optimal solution W, to obtain a preliminary estimate of the source signal. Secondly, the estimated source signal is subjected to CEEMD noise reduction, and after obtaining the modal components of each order, the number of interrelationships is used as a constraint on the modal components, and signal reconstruction is performed. Finally, the signal is subjected to frequency domain feature extraction and bearing fault diagnosis. The experimental results indicate that, the new method successfully captures three fault characteristic frequencies ($1f_i$, $2f_i$, and $3f_i$), with their energy distribution concentrated in the range of 78.9 Hz to 228.7 Hz, indicative of inner race faults. Similarly, when comparing the different results with each other, the denoised source signal spectrum successfully captures the frequencies $1f_o$, $2f_o$, and $3f_o$ and their sideband components, which are characteristic of outer race faults. The sideband components generated in the above spectra are preliminarily judged to be caused by impacts between the fault location and nearby components, resulting in modulated frequency bands where the modulation frequency corresponds to the rotational frequency and its harmonics. Experiments show that the method can effectively diagnose the bearing faults.

Keywords: rolling bearing; fault diagnosis; acoustic signal; blind source separation; CEEMD

MSC: 37M10

check for updates

Academic Editors: Thái Anh Nhan and Istvan Farago

Received: 11 February 2025
Revised: 27 February 2025
Accepted: 2 March 2025
Published: 6 March 2025

Citation: Yan, J.; Zhou, F.; Zhu, X.; Zhang, D. AFSA-FastICA-CEEMD Rolling Bearing Fault Diagnosis Method Based on Acoustic Signals. *Mathematics* **2025**, *13*, 884. https://doi.org/10.3390/math13050884

Copyright: © 2025 by the authors. Licensee MDPI, Basel, Switzerland. This article is an open access article distributed under the terms and conditions of the Creative Commons Attribution (CC BY) license (https://creativecommons.org/licenses/by/4.0/).

1. Introduction

According to recent statistics, bearing failures account for 30% [1] of total failures in rotating machinery equipment. The high interconnectivity and close coupling between equipment are prominent features of modern industrial system machinery. As a result, when a piece of equipment in the system fails or suffers severe damage, it can lead to system downtime, production stoppages, and even trigger unforeseeable safety incidents, thus causing significant economic losses and safety risks for both the enterprise and its workers.

Current research on bearing fault diagnosis primarily relies on vibration signals and acoustic signals. The acquisition of vibration signals is highly dependent on sensors, and, in specific situations, there may be installation difficulties or even the inability to install sensors, which limits their application to some extent. To address the challenge of accurately extracting fault characteristic information from rolling bearing fault signals in the presence of background noise, Wang X et al. [2] proposed the SGMD-FastICA algorithm. The SGMD-FastICA algorithm represents an improved solution that addresses the limitations of the FastICA algorithm, enabling the direct separation of single-channel mixed signals, while also addressing the challenge of proper signal separation in noisy environments. Li J et al. [3] proposed a composite fault diagnosis method for rolling bearings based on compressed sensing (CS) framework. The experiment results show that the method can improve the reconstruction precision and the separation stability of fault signals and can effectively extract fault characteristics and realize the fault diagnosis. Ding H et al. [4] proposed a new method based on wavelet de-noising and nonlinear independent component analysis (ICA) to tackle the nonlinear BSS problem with additive noise. The experimental analysis results show that critical fault vibration source components can be separated by the proposed method, and the fault detection rate is superior to the linear ICA-based approaches.

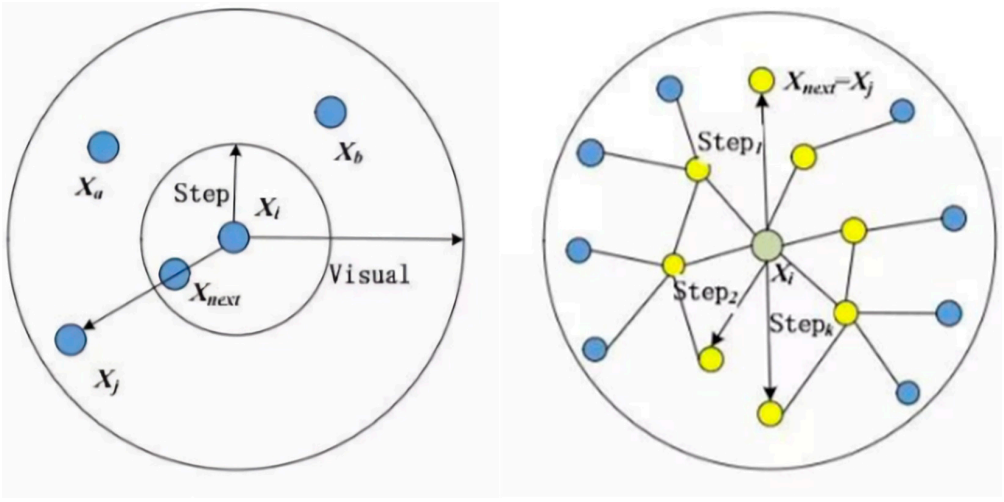
To address the issue of noise contamination in rolling bearing signals, numerous scholars both domestically and internationally have proposed various solutions. However, current methods for bearing signal denoising are relatively limited, with data-processing threshold-based denoising being the mainstream approach. These methods include wavelet analysis, empirical mode decomposition (EMD), variational mode decomposition (VMD), stacked autoencoders, blind source separation, and other denoising techniques [5]. Wang et al. [6] proposed a denoising method combining Singular Value Decomposition (SVD) and VMD to address the significant noise pollution affecting rolling bearing vibration signals in the early stages of fault. This method effectively preserves useful signals and denoises bearing signals in noisy environments. Since vibration signals and acoustic signals share the same source, denoising methods designed for vibration signals can theoretically also be applied to acoustic signals, which forms the theoretical basis for the applicability of vibration-based denoising methods to acoustic signal denoising [7]. Commonly used denoising methods include time-domain denoising [8], frequency-domain denoising [9], and time-frequency domain denoising [10]. Nguyen C D [11] used an adaptive noise canceling technique (ANCT) and distance ratio principal component analysis (DRPCA) to propose a new fault diagnostic model for multi-degree tooth-cut failures (MTCF) in a gearbox operating at inconsistent speeds. To account for background and disturbance noise in the vibration characteristics of gear failures, the proposed approach employs ANCT in the first stage to optimize vibration signals. The experimental results indicate that the proposed model outperforms the state-of-the-art approaches and offers the highest identification accuracy. Saber et al. [12] proposed a threshold denoising method based on empirical mode decomposition, demonstrating the method's effectiveness in signal denoising. Ren et al. [13] introduced an improved EMD-based adaptive noise removal and feature extraction algorithm, and validated its feasibility and effectiveness through both simulation signals and real-world examples. Although EMD has been widely applied in signal denoising, the issue of modal aliasing remains a significant challenge. To address the limitations of EMD, Wu and Huang [14] proposed Ensemble Empirical Mode Decomposition (EEMD) in 2009. EEMD involves adding a finite amplitude of white noise to the signal and performing EMD decomposition on the signal with the added noise, which effectively suppresses the modal aliasing in EMD. Jin et al. [15] proposed a novel denoising method based on local discharge using adaptive EEMD, which outperforms

traditional wavelet and EMD denoising methods in terms of denoising effectiveness. In 2023, Salunkhe V G et al. [16] introduced the Hilbert–Huang transform (HHT) method to diagnose the unbalanced rolling bearing faults of rotating machinery. The HHT approach is experimentally proven with the unbalance diagnosis and is capable of classifying marginal Hilbert spectra distribution. Because of its superior time–frequency characteristics and pattern identification of marginal Hilbert spectra and fault indicator indices, the newly stated HHT can process nonlinear, non-stationary, and even transient signals. The findings demonstrate that the suggested method is superior in terms of unbalance fault identification accuracy for monitoring the dynamic stability of industrial rotating machinery.

2. Theoretical Background

2.1. Artificial Fish Swarm Algorithm

Let us assume that in a certain space, there exists a swarm consisting of N artificial fish. Let the current state of the artificial fish be represented by the vector $X = (x_1, x_2, x_3, \ldots, x_n)$, where $x_i (i = 1, 2, \ldots, n)$ denotes the optimization variables [17]. Assume that the fitness of the environment state in which the artificial fish is located is $Y = f(X)$, and $f(X)$ is the fitness function. Let $d = \left\| x_i - x_j \right\|$ represent the distance between the individual artificial fish. The visual perception range of the artificial fish is denoted by Visual, the number of attempts made by the artificial fish during each foraging behavior is represented by try-number, and Step denotes the step size of the artificial fish's movement. Rand() represents the random selection behavior executed by the artificial fish during its wandering phase. Delta δ is the crowding factor [18], and the visual model of the artificial fish is shown in Figure 1.



(**a**) (**b**)

Figure 1. Artificial Fish Swarm Algorithm Model: (**a**) Continuous Vision Model, (**b**) Discrete Vision Model.

2.1.1. Foraging Behavior

Let the current state of the artificial fish be represented by X_i, and assume that within its visual range, there exists another state X_i that is randomly selected by the artificial fish. The state X_i can be described as follows:

$$X_j = X_i + Visual * Rand() \quad (1)$$

The fitness values of state X_i and X_j are calculated. If the fitness value of Y_j is greater than that of Y_i, the artificial fish will move one step toward Y_j, which can be expressed as:

$$X_i^{t+1} = X_i^t + \frac{X_j - X_i^t}{\|X_j - X_i^t\|} * Step * Rand() \quad (2)$$

If the fitness value of state Y_j is less than that of Y_i, the artificial fish will continue searching for a new state X_j within its visual range and perform the same evaluation. If no better state is found after try-number attempts, the artificial fish will execute a random wandering behavior, randomly selecting a new state.

2.1.2. Swarming Behavior

Let the current state of the artificial fish be X_i, and within $d_{ij} < visual$ visual range, there are n_f swarm mates, with the center of the swarm denoted as X_c. If $Y_c/n_f < \delta Y_i$, the artificial fish at state X_i will move toward the center X_c. If $Y_c/n_f > \delta Y_i$, the artificial fish will perform foraging behavior. This process can be expressed as:

$$X_i^{t+1} = X_i^t + \frac{X_c - X_i^t}{\|X_c - X_i^t\|} * Step * Rand() \quad (3)$$

2.1.3. Rear-End Collision Behavior

Let the current state of the artificial fish be X_i, and within $d_{ij} < visual$ visual range, there are n_f swarm mates, Among them, there is a school of fish, Partner Y_j, with the highest function value. If $Y_c/n_f < \delta Y_i$, this indicates that the area around the best fish school partner is not crowded. At this point, the artificial fish in state X_i will move toward partner X_j; otherwise, it will continue its foraging behavior. The above process can be expressed as:

$$X_i^{t+1} = X_i^j + \frac{X_j - X_i^t}{\|X_j - X_i^t\|} * Step * Rand() \quad (4)$$

2.1.4. Random Behavior

Random behavior refers to a supplementary behavior to the foraging behavior, where the artificial fish move randomly within a unit of visual range. When a better fitness is found, the fish will quickly move toward the direction with higher fitness. If the condition is still not met after a certain number of attempts, the artificial fish will randomly select a state within its perception range. This process can be expressed as:

$$X_i^{t+1} = X_1^t + Visual * Rand() \quad (5)$$

2.1.5. Billboard

The **billboard** is used to record the fitness values of individual artificial fish. After each iteration, the current state information of the fish is compared with the historical data on the billboard [19]. If the current state has a better fitness value, it will update the information on the billboard; otherwise, it remains unchanged. After the iteration is complete, the values on the billboard represent the optimal solution. Common methods to evaluate convergence include assessing the range of acceptable errors based on the mean squared deviation of several consecutive small fish, evaluating whether the number of artificial fish in a specific area has reached a predetermined proportion, checking whether the average value of multiple consecutive calculations does not exceed the previously found maximum, or limiting the maximum number of iterations [20].

2.2. The Fast Independent Component Analysis (Fast ICA) Algorithm

Assume there are n unknown source signals $S(t) = [s_1(t), s_2(t), \ldots, s_n]^T$, and $X(t) = [x_1(t), x_2(t), \ldots, x_n]^T$ is a column vector composed of m mixed signals, which are randomly mixed from n source signals, as described in [21]. Then, the following equation must hold:

$$X(t) = AS(t) \tag{6}$$

In this case, A is referred to as the mixing matrix. The practical meaning of this equation is that any mixed signal x_n is a linear transformation [22] of A by some matrix $S(t)$. We can further deduce that the solution to this equation is not unique, and therefore the decomposition result is also non-unique. Thus, independent component analysis must satisfy the following conditions:

1. The source signal matrix $S(t)$ can only contain one source signal with a Gaussian distribution probability density function [23]; if there are multiple such signals, they cannot be separated.
2. The components of the source signal matrix $S(t)$ must be linearly independent, meaning that the source signal matrix $S(t)$ must be of full rank.
3. The source signal matrix $S(t)$ [24] and the mixing signal matrix [25] must have the same dimensionality, i.e., $n = m$.

Rewriting Equation (6) as a matrix equation:

$$\begin{bmatrix} x_1(t) \\ x_2(t) \\ \vdots \\ x_m(t) \end{bmatrix} = \begin{bmatrix} a_{11} & \cdots & a_{1n} \\ \vdots & \ddots & \vdots \\ a_{n1} & \cdots & a_{nn} \end{bmatrix} \begin{bmatrix} s_1(t) \\ s_2(t) \\ \vdots \\ s_n(t) \end{bmatrix} \tag{7}$$

In this case, $X(t)$ is the matrix containing m mixed signals, and $S(t)$ is the matrix containing n unknown source signals. When noise is present in the environment, Equation (7) should be written as:

$$\begin{bmatrix} x_1(t) \\ x_2(t) \\ \vdots \\ x_m(t) \end{bmatrix} = \begin{bmatrix} a_{11} & \cdots & a_{1n} \\ \vdots & \ddots & \vdots \\ a_{n1} & \cdots & a_{nn} \end{bmatrix} \begin{bmatrix} s_1(t) \\ s_2(t) \\ \vdots \\ s_n(t) \end{bmatrix} + \begin{bmatrix} n_1(t) \\ n_2(t) \\ \vdots \\ n_m(t) \end{bmatrix} \tag{8}$$

In this case, $N(t)$ is the matrix containing m noise signals.

From the above reasoning, it is clear that in order to separate the source signals from the mixed signals, we must find the demixing matrix W, where W is the inverse of the mixing matrix A, i.e., $W = A^{-1}$. Since $S(t)$ is of full rank [23], the demixing matrix W has a unique solution. Let $Y(t) = [y_1(t), y_2(t), \ldots, y_n]^T$ be the estimate of the source signals $S(t)$, and the expression for $Y(t)$ is:

$$Y(t) = WX(t) + N(t) \tag{9}$$

From the above equation, it can be seen that when there is no noise interference in the environment, $Y(t) = S(t)$ holds. However, when noise interference is present in the environment, the obtained source signals will also be affected by noise, because:

$$\begin{bmatrix} w_{11} & \dots & w_{1n} \\ \vdots & \ddots & \vdots \\ w_{n1} & \dots & w_{nn} \end{bmatrix}^{-1} \left(\begin{bmatrix} x_1(t) \\ x_2(t) \\ \vdots \\ x_m(t) \end{bmatrix} - \begin{bmatrix} n_1(t) \\ n_2(t) \\ \vdots \\ n_m(t) \end{bmatrix} \right) = \begin{bmatrix} s_1(t) \\ s_2(t) \\ \vdots \\ s_n(t) \end{bmatrix} \tag{10}$$

The FastICA algorithm is essentially based on the maximum entropy principle [26]. Its main objective is to minimize the information between the estimated components using neural network techniques, in order to approximate negative entropy.

$$J(x) = H(x_{gauss}) - H(x) \tag{11}$$

Using the probability density function of the signals [27], the following expression is the approximate expression for negative entropy based on the maximum entropy principle:

$$J(x) \approx k_1(E(G_1(x)))^2 + k_2(E(G_2(x))) - E(G_2(v))^2 \tag{12}$$

where G_1 and G_2 are non-quadratic functions, k_1 and k_2 are considered positive constants, and v is a zero-mean, unit-variance Gaussian variable. When there is a non-quadratic function, we have:

$$J(x) \propto (E(G_2(x))) - E(G_2(v))^2 \tag{13}$$

Commonly used non-quadratic functions include:

$$G_1(x) = \frac{1}{a} \lg \cosh ax \tag{14}$$

$$G_3(x) = x^4/4 \tag{15}$$

$$G_2(x) = -\exp(-x^2/2) \tag{16}$$

where a is a constant between 1 and 2, and typically $a = 1$ is a constant.

Once the contrast function is determined, the objective function will converge as quickly as possible toward the direction of non-Gaussian maximization. When the source signal $s(t)$ undergoes a linear transformation [28], the mixed signal $x(t)$ is obtained, i.e., $x(t) = As(t)$, and A form a mixing matrix. Finally, after mean removal and whitening processing [29], the resulting mixed signal $v(t)$ is written as:

$$v(t) = Qx(t) = QAs(t) = Ws(t) \tag{17}$$

In the equation, Q is the whitening matrix, A is the mixing matrix, and W is the orthogonal separation matrix. By computing W and finding its inverse transformation W^{-1}, the estimated source signals $y(t)$ can be obtained as:

$$y(t) = W^T v(t) = W^T W s(t) = s(t) \tag{18}$$

Then, the negative entropy is maximized:

$$J_G(W) = [E(G(W^T x)) - E(G(v))]^2 \tag{19}$$

In the equation, x is the mixed signal, and v is a Gaussian variable with zero mean and unit variance. When $E((W^T x)^2) = \|W\|^2 = 1$ is true, the optimal point of the following equation can be obtained:

$$E(xg(W^T x)) + \beta W = 0 \tag{20}$$

In the equation, $g()$ is the derivative of $G()$, $G()$ is a non-quadratic function, and β is a constant.

Then, using Newton's iteration method [30] to solve for W, the approximate iteration is obtained as:

$$W_{k+1} = W_k - [E(xg(W^T x)) + \beta W]/[E(g(W^T X)) + \beta] \quad (21)$$

Substituting $E(g(W^T x)) + \beta$ into both sides of Equation (16), we obtain:

$$W_{k+1} = E(xg(W^T x)) - E(g(W^T x))W \quad (22)$$

The general process of the FastICA algorithm can be expressed as (Figure 2):

step1Collect the corresponding target device signals.

step2Center the collected mixed signals to obtain data with a mean of 0 and a standard deviation of 1, following a standard normal distribution.

step3The whitened mixed signals are processed after centering. Whitening can eliminate the correlation between the mixed signals.

step4The W matrix is initialized with random weights [31], and the nonlinear function G is introduced into the algorithm.



Figure 2. FastICA Algorithm Process.

Perform Newton's iteration, calculate, and check whether it has converged to the direction of non-Gaussian maximization. If it has converged, update the W matrix parameters and obtain the separated source signals from $W_{k+1} = E(xg(W^T x)) - E(g(W^T x))W$. If it has not converged, repeat the Newton iteration until the W matrix converges.

2.3. CEEMD Denoising Method

Empirical Mode Decomposition (EMD) is effective in processing nonlinear and non-stationary signals [32], especially when applied to blind source separation tasks. The EMD algorithm continuously decomposes the original signal until it obtains intrinsic mode functions (IMFs) that satisfy the required conditions. However, the IMFs decomposed by the EMD algorithm often suffer from mode mixing [33], and the computation efficiency is relatively low. To address this issue, the Ensemble Empirical Mode Decomposition (EEMD) algorithm was developed based on EMD. The EEMD algorithm adds Gaussian white noise [34] to the signal, thereby altering the extremal points of the original signal. The impact of the added white noise is then canceled out by averaging over the ensemble, effectively resolving the mode mixing problem present in the EMD algorithm. While the EEMD algorithm significantly improves the mode mixing issue, it still has certain limitations. The number of iterations and the amplitude of the added white noise in the EEMD algorithm are set empirically, which leads to a significant degree of uncertainty in the decomposition results. Based on the EEMD algorithm, the Complementary Ensemble Empirical Mode Decomposition (CEEMD) algorithm [35] was developed as an improvement.

In 2010, Yeh et al. [36] proposed Complementary Ensemble Empirical Mode Decomposition (CEEMD) based on EEMD. To eliminate the redundant auxiliary white noise in the reconstructed signal after EEMD decomposition, this method introduces a pair of opposite-sign white noises (positive and negative) as auxiliary noise in the source signal. This not only reduces the number of iterations in the decomposition process but also effectively lowers the computational cost. The signal decomposition steps in CEEMD are similar to those in EEMD, with the main difference being the type of white noise added.

(1) Let the number of ensemble averages be N, and the number of signal aggregations be I. We add a white-noise time series to the original-signal time series, successfully constructing two entirely new time series:

$$\begin{cases} P_i(t) = x(t) + n_i(t) \\ N_i(t) = x(t) - n_i(t) \end{cases} \tag{23}$$

where $P_i(t)$ and $N_i(t)$ are the new signals generated after adding white noise for the i time, and $n_i(t)$ is the white noise signal added during the i decomposition step of the n experiment.

(2) Introduce $p_i(t)$ and $N_i(t)$ into the CEEMD algorithm, perform I decompositions, and obtain the components.

$$P_i(t) = \sum_{i}^{I} a_{n,i}, N_i(t) = \sum_{i}^{I} a'_{n,i} \tag{24}$$

where $a_{n,i}$ and $a'_{n,i}$ are the two sets of IMF components obtained from the i decomposition of the n iteration.

(3) Repeat step (2) until $i = I$ is achieved.

(4) Calculate the overall average component value IMF_n^{avg} of the $a_{n,i}$ component from the I CEEMD decomposition in the n iteration:

$$IMF_n^{avg} = \frac{1}{2I} \sum_{i=1}^{I} (a_{n,i} + a'_{n,i}) \tag{25}$$

(5) Obtain the overall average value IMF^{avg}:

$$IMF^{avg} = \frac{1}{N}\sum_{n=1}^{n} IMF_n^{avg} \tag{26}$$

The algorithm flow is roughly as shown in Figure 3.

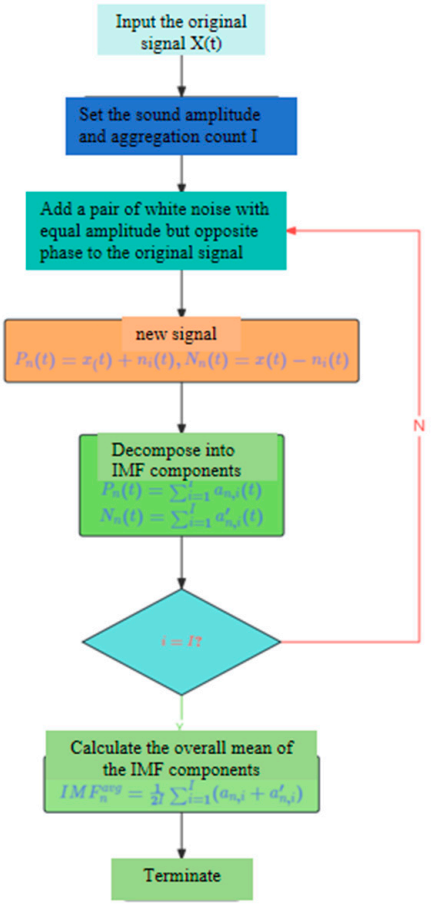


Figure 3. CEEMD Flowchart.

2.4. Cross-Correlation Coefficient

The correlation coefficient is used to describe the dependency relationship between the vibration amplitudes of two signals, and it has a significant advantage in extracting information from signals that are affected by noise. The cross-correlation coefficient is the maximum value of the cross-correlation function. Let there be signals $x(t)$ and $y(t)$, then the cross-correlation function $R_{xy}(\tau)$ of the two signals can be expressed as:

$$R_{xy}(\tau) = \lim_{T\to\infty}\frac{1}{T}\int_0^T x(t)y(t+\tau)dt \tag{27}$$

where T is the time series, and τ is the bias. Then, the correlation coefficient $\rho_{xy}(\tau)$ can be expressed as:

$$\rho_{xy}(\tau) = \frac{R_{xy}(\tau)}{\sigma_x\sigma_y} \tag{28}$$

where σ_x is the standard deviation of signal $x(t)$, and σ_y is the standard deviation of signal $y(t)$.

When the cross-correlation between two signals is higher, the degree of association between the signals is greater. Therefore, the cross-correlation coefficient can be used

to filter the IMF components generated by CEEMD. IMF components with low cross-correlation coefficients are discarded, and the remaining IMF components are used for signal reconstruction [37]. This method effectively filters out noise from the signal.

3. The ASFA-FastICA-CEEMD Framework

The proposed method framework is shown in the following Figure 4, and the process is as follows:

(1) In the FastICA module, set the number of components and initialize the mixing matrix W.
(2) Substitute W into the approximate expression of negative entropy to obtain:

$$W_{k+1} = E(xg(W^T x)) - E(g(W^T x))W \tag{29}$$

(3) In the AFSA module, construct the cost function [38] based on the condition $E((W^T x)^2) = \|W\|^2 = 1$.

$$J(W) = E[G(W^T x)] + \lambda(\|W\|^2 - 1)^2 \tag{30}$$

among them:

$$j'(W) = E[xx^T j'(W^T(t))]x + E[W^T x g(W^T x)] \tag{31}$$

(4) Initialize the fish swarm and set the number of iterations for the random behavior execution.
(5) Search for the maximum point of $E[G(W^T x)]$.
(6) Obtain the global optimal solution of the W matrix, and perform the inverse transformation [39] to obtain the estimated source signal.
(7) Perform CEEMD modal decomposition on the estimated source signal.
(8) Compare the obtained modal components using the cross-correlation coefficient [40], and discard those with a cross-correlation coefficient less than 0.1. Use the remaining components [40] for signal reconstruction.
(9) Perform a Fast Fourier Transform (FFT) on the reconstructed signal to extract frequency-domain features, and use the frequency-domain feature information [41] for fault diagnosis.

In the AFSA module, the global optimal solution for the mixing matrix W is searched through the behavior simulation of the fish swarm. The optimization process can be divided into the following steps:

(1) **Constructing the cost function**: AFSA constructs a cost function $J(W) = E[G(W^T x)] + \lambda(\|W\|^2 - 1)^2$ using condition $E((W^T x)^2) = \|W\|^2 = 1$. This cost function is typically associated with FastICA's objective function (such as negative entropy or a similar optimization goal). The goal of the cost function $E((W^T x)^2) = \|W\|^2 = 1$ is to minimize the system's energy, thereby optimizing the mixing matrix W.
(2) **Initializing the fish swarm**: In AFSA, a fish swarm is initialized, where each fish represents a potential solution (i.e., a candidate value for the mixing matrix W).
(3) **Random behavior and search**: Each fish in the swarm performs random movements in the solution space based on its behaviors (such as foraging, following, etc.). Each fish adjusts its position according to the value of the cost function $E((W^T x)^2) = \|W\|^2 = 1$, moving closer to a better solution.
(4) **Searching for the maximum point**: After several random movements and local searches, the fish swarm gradually concentrates on the maximum point in the solution space, thereby obtaining the global optimal solution for the mixing matrix W.

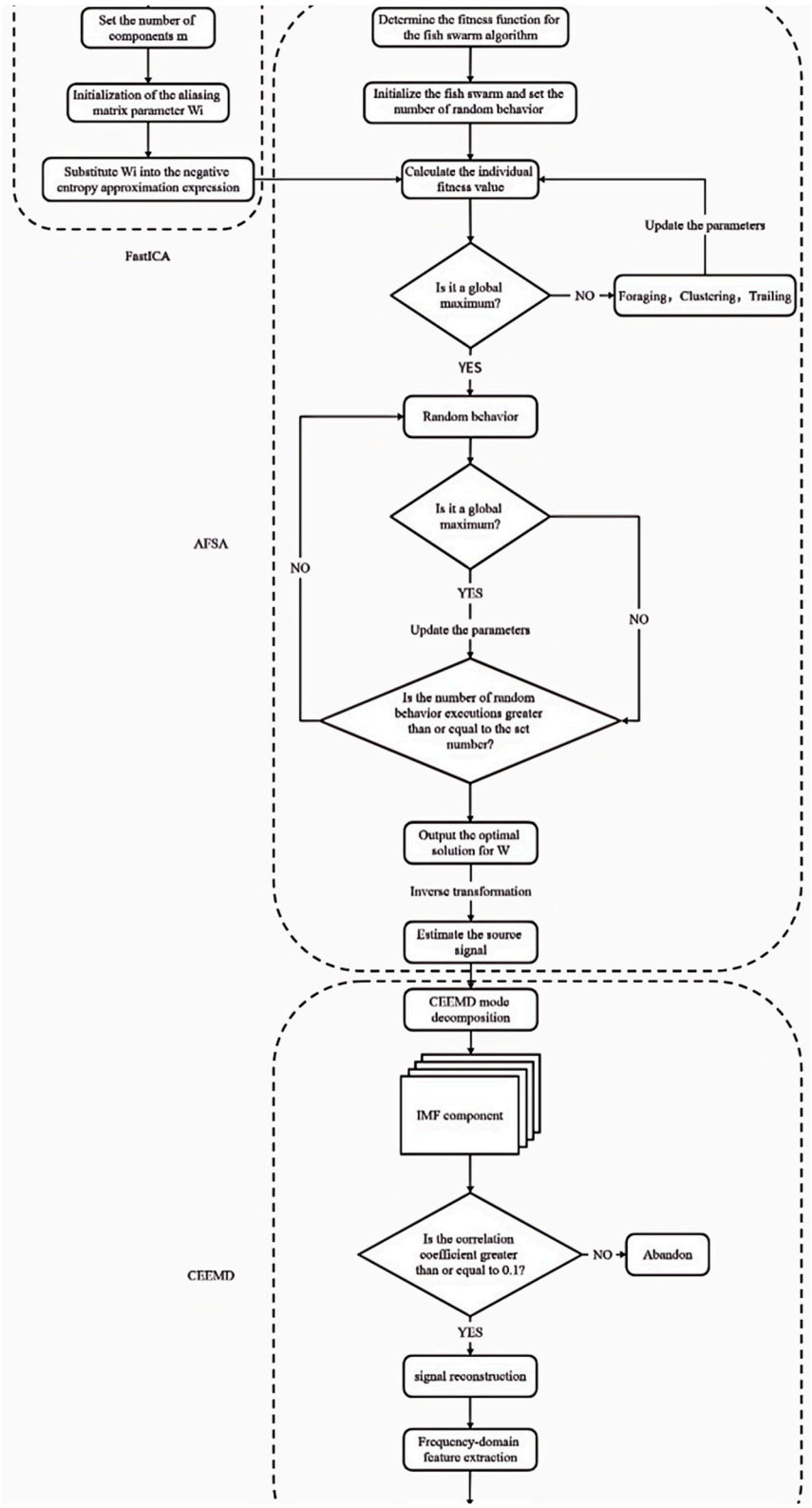


Figure 4. ASFA-FastICA-CEEMD.

4. Simulation Experiments

4.1. AFSA-FastICA Simulation Experiment

In this Section, we validate the fish swarm algorithm-based acoustic signal separation method using four simulated signals, three of which are:

$$s_1 = 1.5\sin(0.4\pi t) \tag{32}$$

$$s_2 = 3sawtooth(0.12\pi x) + \sin(0.12\pi x) \tag{33}$$

$$s_3 = 2sawtooth(0.7\pi x) \tag{34}$$

The other is a random signal.

The waveform of the four source signals is shown in Figure 5.

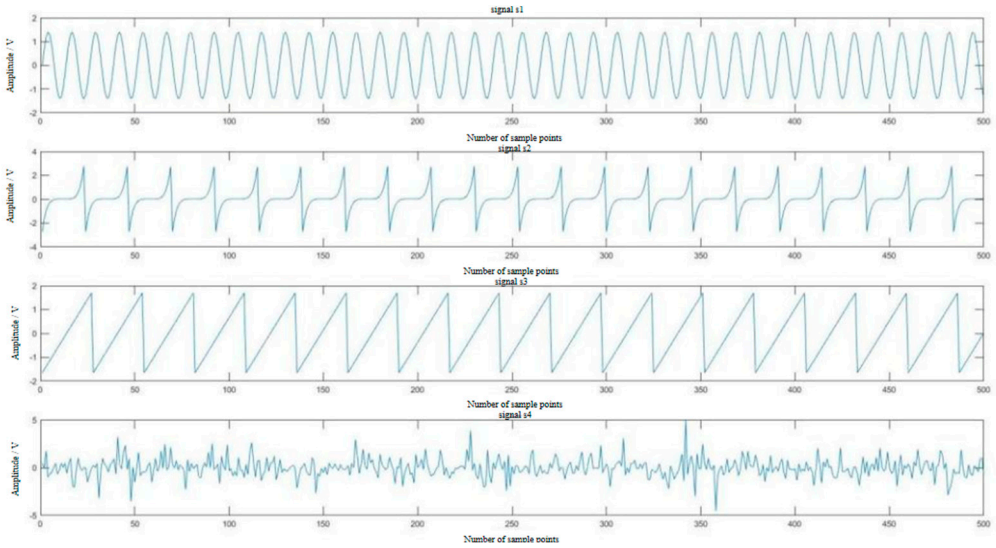


Figure 5. Source Signals.

The signals are mixed using the estimated matrix A, and the mixed signals are shown in Figure 6.

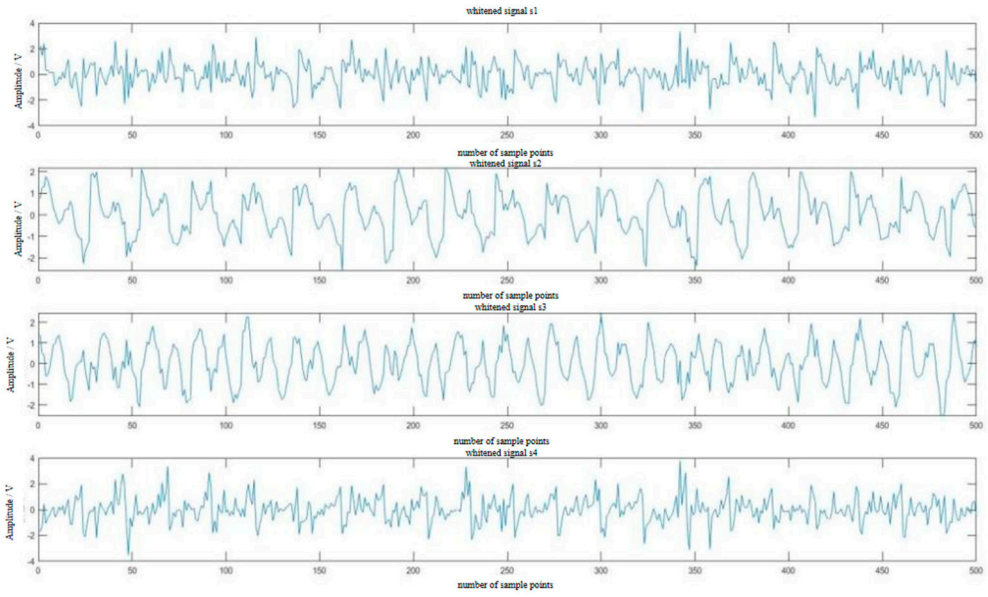


Figure 6. Mixed Signals.

The similarity comparison between the separated signals of the two methods and the source signals is shown in Tables 1 and 2.

Table 1. Separation Similarity of the Artificial Fish Swarm Algorithm.

S_1	99.70%	99.60%	99.70%	99.80%	99.50%	99.60%	99.80%	99.80%	99.50%	99.60%
S_2	98.80%	99.70%	99.70%	99.80%	99.50%	99.70%	99.60%	99.80%	99.60%	99.60%
S_3	99.80%	99.70%	99.70%	99.80%	99.70%	99.70%	99.60%	99.80%	99.60%	99.60%
S_4	98.50%	98.50%	98.50%	98.50%	98.50%	98.50%	98.50%	98.50%	98.50%	98.50%

Table 2. Separation Similarity of the FastICA Algorithm.

S1	98.40%	99.50%	98.60%	99.70%	98.40%	98.40%	98.50%	98.50%	99.70%	99.00%
S2	98.60%	99.50%	99.60%	99.70%	99.50%	99.40%	99.10%	99.50%	98.90%	98.40%
S3	99.40%	96.80%	96.60%	90.70%	90.40%	95.40%	95.10%	95.10%	94.70%	99.70%
S4	99.70%	96.80%	96.60%	98.20%	98.40%	98.40%	97.80%	97.70%	98.20%	97.90%

As shown in Figures 7 and 8, the convergence speed of the Artificial Fish Swarm Algorithm is clearly faster, converging after approximately 33 iterations. From the figure, it can be observed that the loss curve of the Artificial Fish Swarm Algorithm [42] decreases more smoothly. Although there are small fluctuations near the convergence value, the fish swarm algorithm benefits from the crowding degree [19] in the judgment of Y_c/n_f, which results in a shorter fluctuation interval and fewer iterations experiencing such fluctuations. This indicates that the algorithm does not remain trapped in a local optimum for an extended period. In contrast, FastICA experiences fluctuations at different points, suggesting that it is more prone to getting stuck in a local optimum, which leads to a slower convergence speed, with convergence occurring around 44 iterations (Figures 9–11).

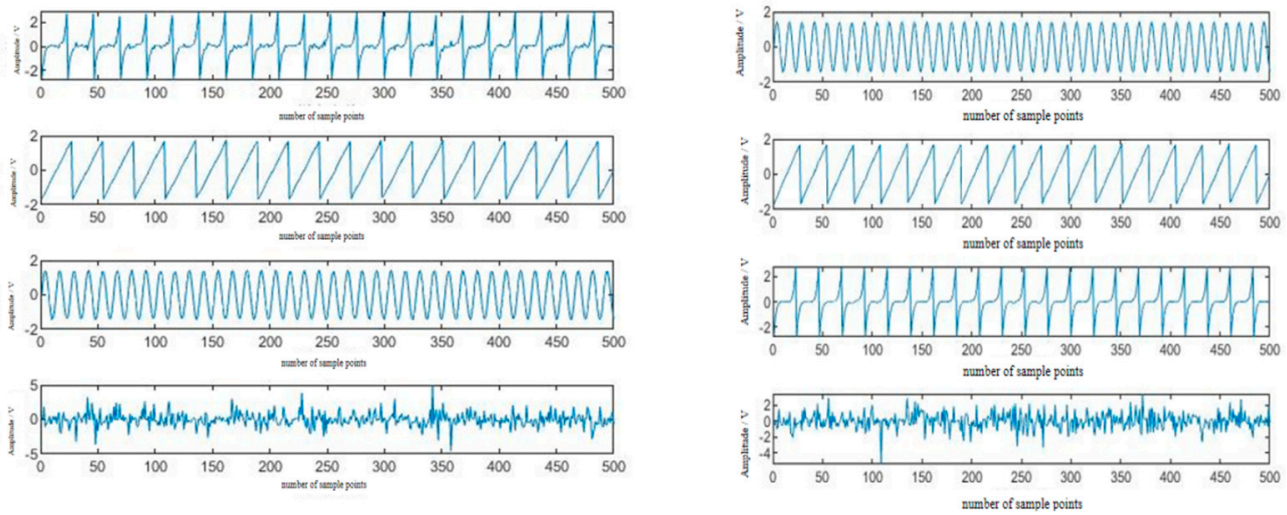


Figure 7. Acoustic Separation Signals Based on the Artificial Fish Swarm Algorithm.

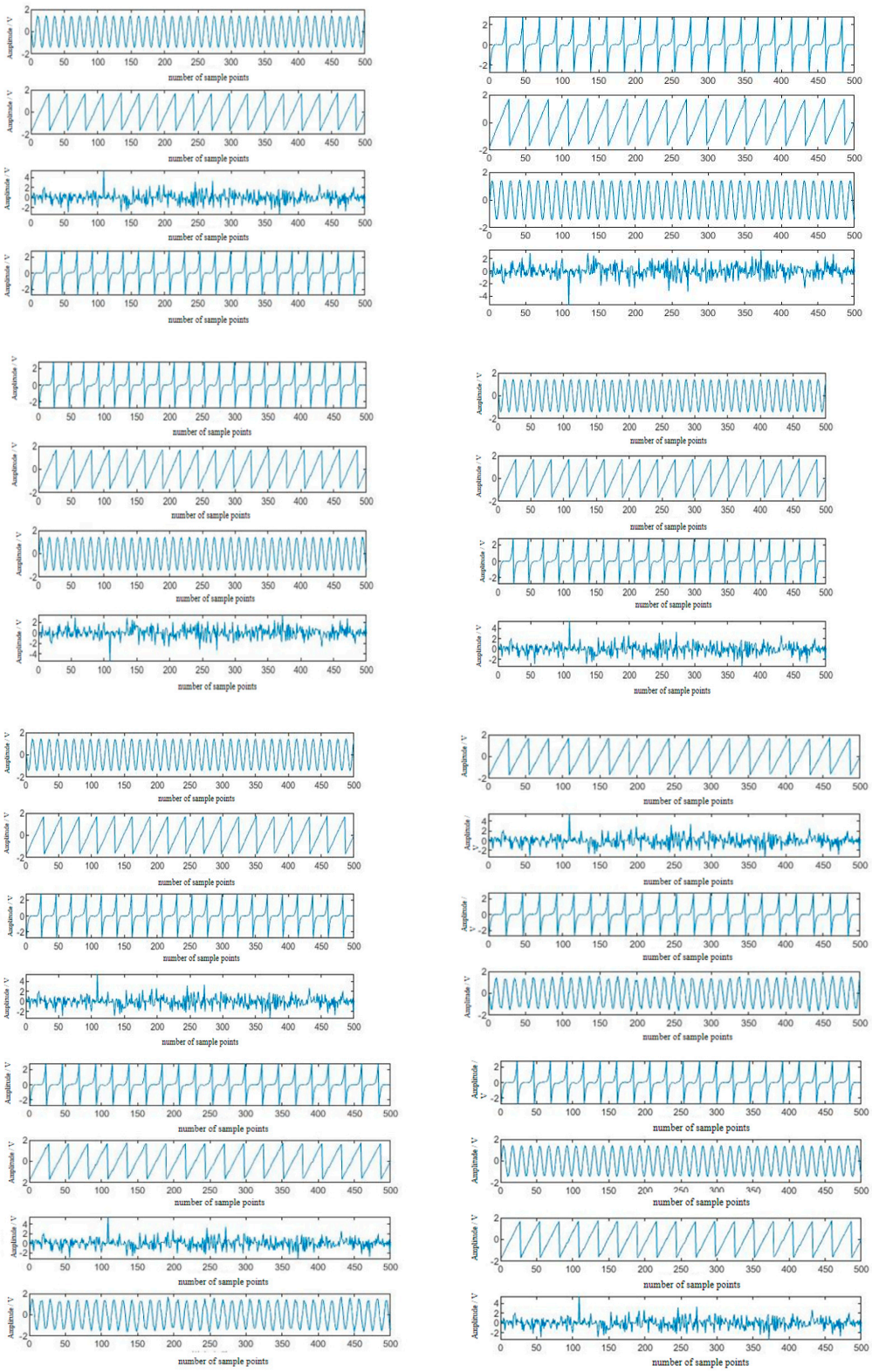


Figure 8. Continuation of Acoustic Separation Signals Based on the Artificial Fish Swarm Algorithm.

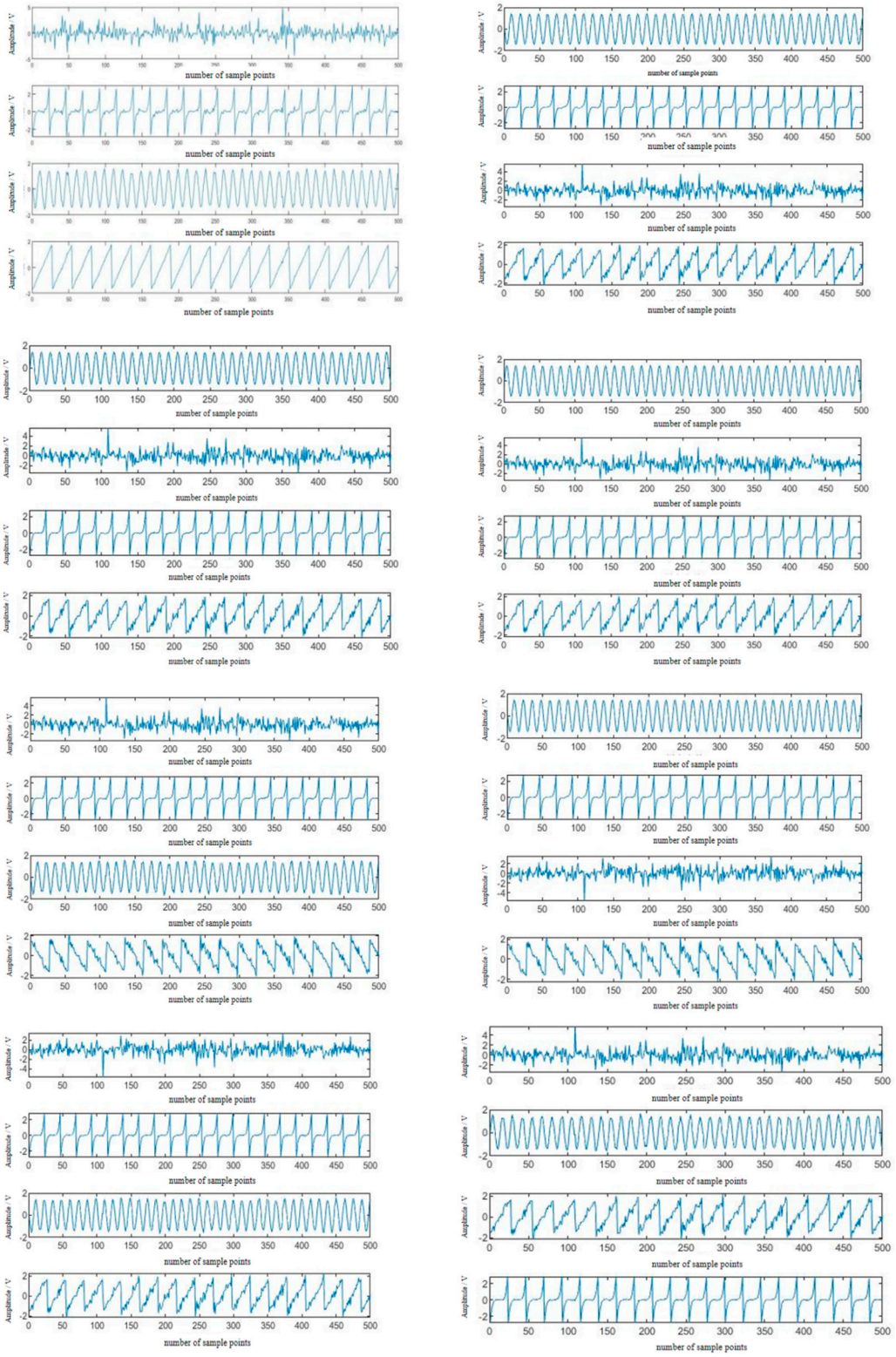


Figure 9. FastICA Acoustic Separation Signals.

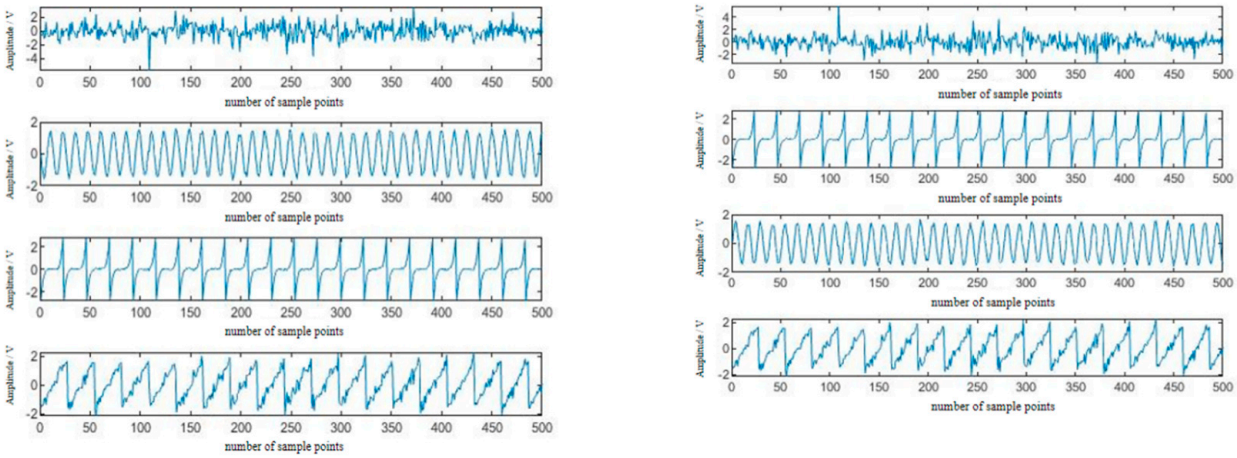


Figure 10. Continuation of FastICA Acoustic Separation Signals.

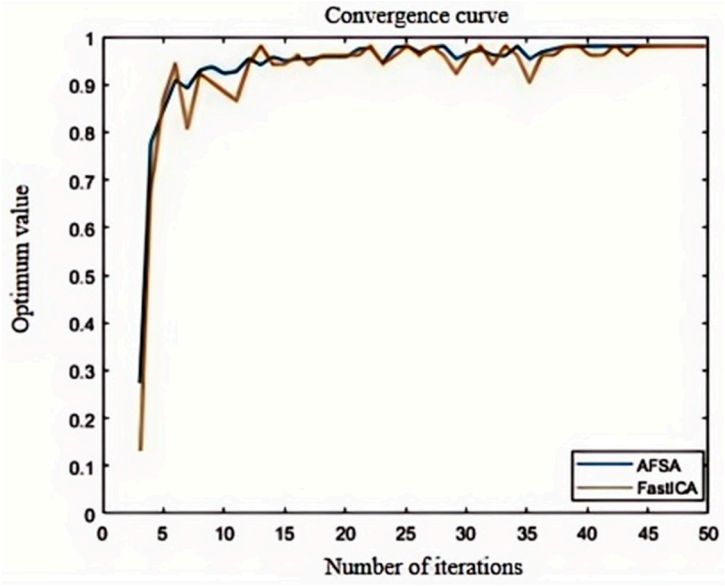


Figure 11. Artificial Fish Swarm Algorithm vs. Original FastICA Algorithm.

4.2. The CEEMD Denoising Simulation Experiment

In order to effectively validate the above points and the effectiveness of the CEEMD algorithm, we use the following simulated signal for the experiment:

$$x_1 = 2\sin(60\pi t + \pi/2) \tag{35}$$

$$x_2 = \sin(16\pi t + \pi/3) \times (t+1) \tag{36}$$

Here, an additional random signal $n(t)$ with a sampling frequency $N = 1000$ is included.

The above signals are then aliased, resulting in an intermittent interference signal [43]:

$$S_1 = x_1 + x_2 + n(t) \tag{37}$$

The time-domain waveform of the simulated signal is shown in Figure 12a, and the decomposed signals using EMD, EEMD, and CEEMD are shown in Figure 12b, Figure 12c, and Figure 12d, respectively.

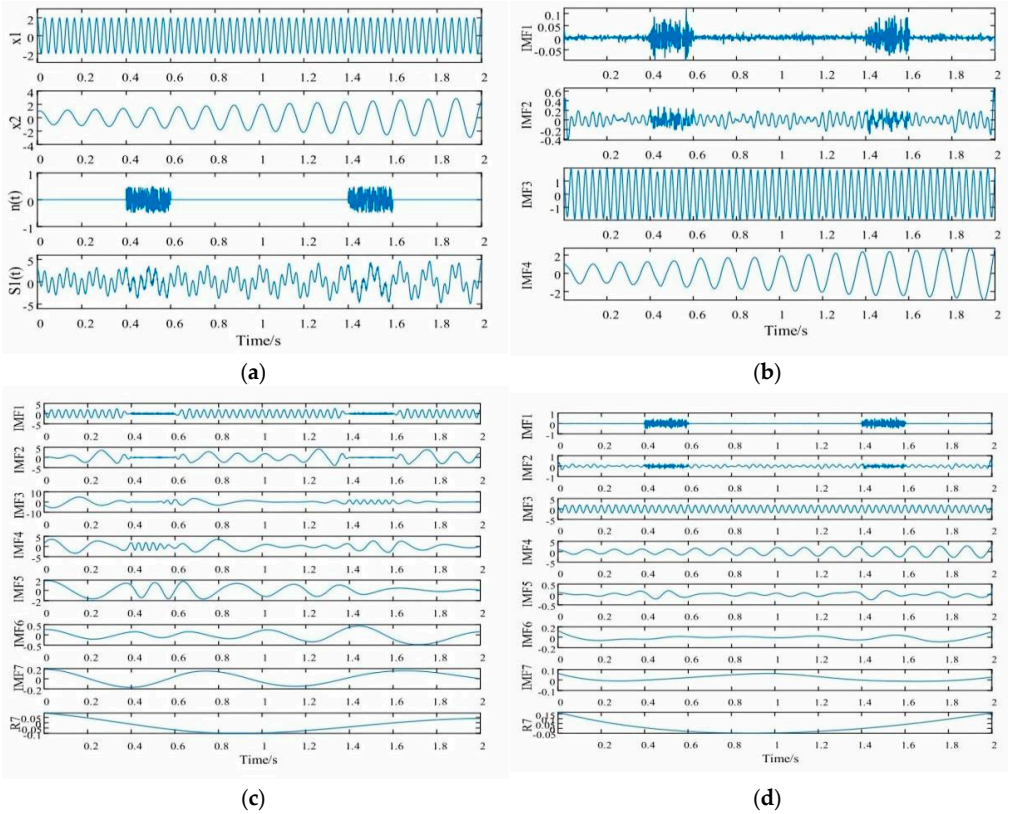


Figure 12. Time-Domain Waveform of Simulated Signal and Decomposed Signals. (**a**) Time-domain waveform of the simulated signal, (**b**) CEEMD decomposed signal, (**c**) EMD decomposed signal, (**d**) EEMD decomposed signal.

As shown in Figure 12b, the IMF1 of CEEMD exhibits the characteristics of an intermittent signal [44], but it experiences slight fluctuations where the amplitude of the source signal is zero. IMF2 corresponds to a spurious component [45], IMF3 displays the characteristics of a periodic signal, and IMF4 exhibits the characteristics of a signal with variable amplitude [45]. Figure 12c shows the EMD decomposed signal. From the figure, it is evident that due to the interference of noise signals, EMD suffers from significant mode mixing, and many spurious components appear. Figure 12d shows the EEMD decomposed signal. Under the influence of white noise and ensemble averaging, the mode mixing is greatly improved compared to the EMD decomposed signal; however, IMF2 still exhibits mode mixing. IMF3 and IMF4 represent periodic signal characteristics [32] and variable amplitude signal characteristics, respectively, while the remaining components are spurious.

By comparing the completeness and orthogonality [46] of the EMD, EEMD, and CEEMD algorithms, it is clear that CEEMD has the best orthogonality, and its completeness is also superior to that of EMD and EEMD. Therefore, CEEMD exhibits the least mode mixing, as shown in Table 3.

Table 3. Comparison of Decomposition Method Performance.

	Orthogonality	Completeness	Aliasing
EMD	0.085	0.0036	obvious
EEMD	0.072	0.0042	exist
CEEMD	0.034	0.0061	minimum

5. Experiment

5.1. Experimental Equipment Parameters

The bearing test platform used in this experiment is shown in Figure 13, and the bearing parameters are listed in Table 4. The fault frequencies [47] are shown in Table 5, with the motor's rated speed being 800 rpm. The array of acoustic signal sensors [48] used is shown in Figure 14, and their performance parameters are listed in Table 6. The experiment was conducted using bearings with rolling element faults, inner race faults, outer race faults, and cage faults.

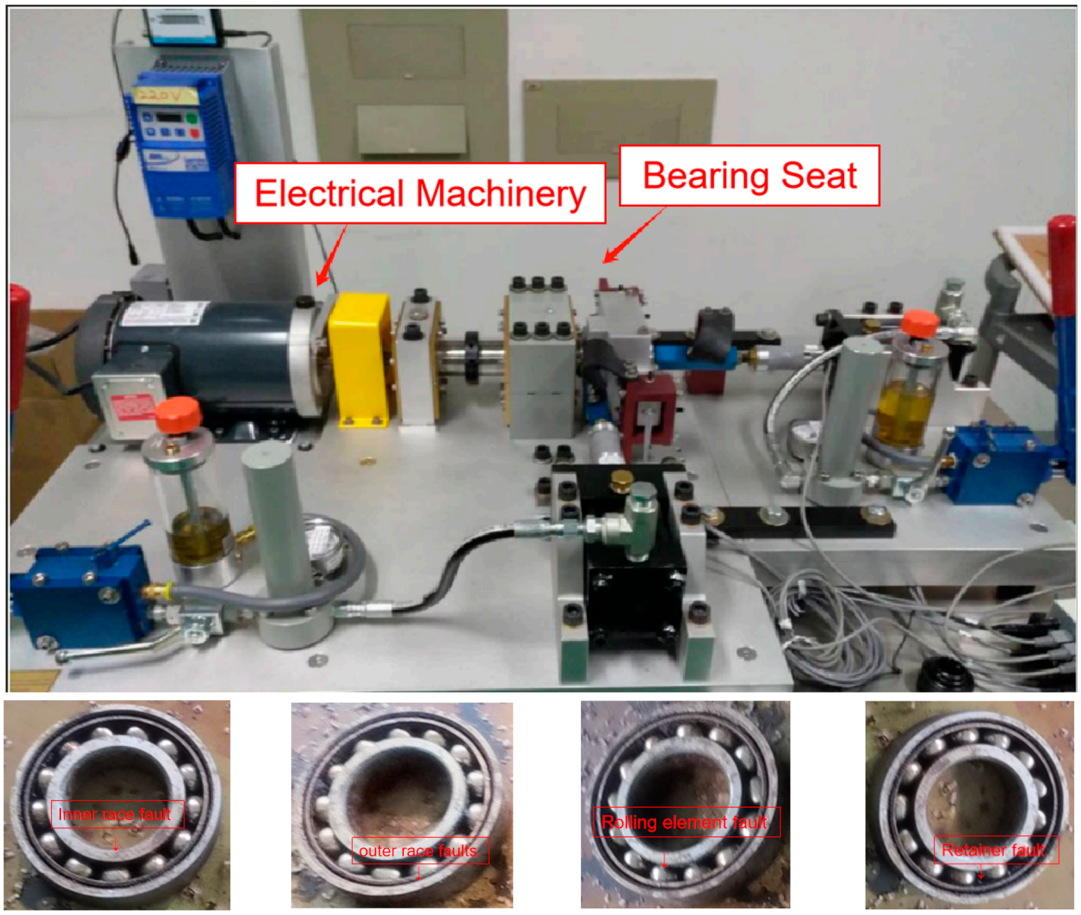


Figure 13. Bearing Fault Test Platform.

Table 4. Bearing Parameters.

Outer Ring Diameter R/mm	Inner Ring Diameter R/mm	Pitch Diameter D/mm	Ball Diameter D/mm	Number of Rolling Elements Z	Contact Angle α
90	40	65	22	9	0

Table 5. Fault Characteristic Frequencies.

Bearing Components	Outer Ring f_o	Inner Ring f_i	Rolling Element f_r	Cage f_c
Fault frequency	$2.97f$	$6.02f$	$3.98f$	$0.33f$

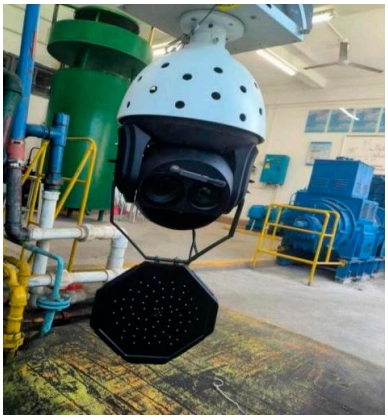


Figure 14. Acoustic Signal Sensor Array.

Table 6. Acoustic Signal Sensor Array Parameters.

Number of Pickups	Pickup Distance m	Sampling Rate KHz	Frequency Range KHz	Maximum Sound Pressure dB	Sensitivity dBFS	Refresh Rate FPS	Distortion Rate %
64	50 m	192 KHz	20 Hz~96 KHz	220 dB	−26 dBFS	25 FPS	THD < 1%

5.2. Experimental Procedure

In order to intuitively compare the impact of the Artificial Fish Swarm Algorithm (AFSA) for acoustic signal separation on rolling bearing fault diagnosis, we first collected the acoustic signals of rolling bearings under four different operating conditions. At the same time, other onsite mechanical equipment, such as air compressors, diesel generators, and marine oil extraction machines, were also turned on. The time-domain waveform and spectral features of these signals are shown in Figure 15. Then, the collected signals were input into the blind source separation algorithm optimized by the Artificial Fish Swarm Algorithm. The resulting time-domain waveform is shown in Figure 16, and the spectral features [49] are presented in Figure 17.

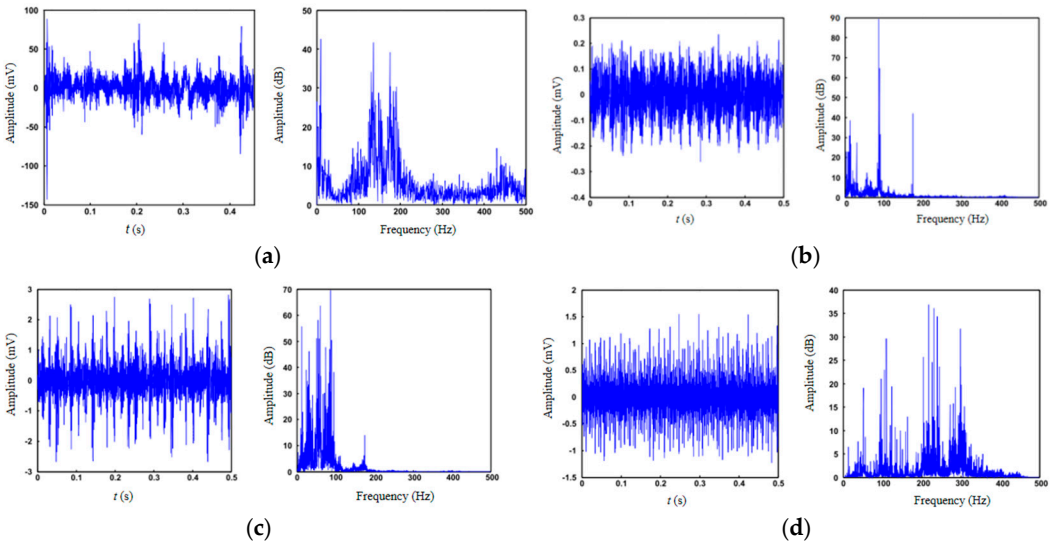


Figure 15. Without Acoustic Signal Separation: (**a**) Rolling element fault, (**b**) Cage fault, (**c**) Inner race fault, (**d**) Outer race fault.

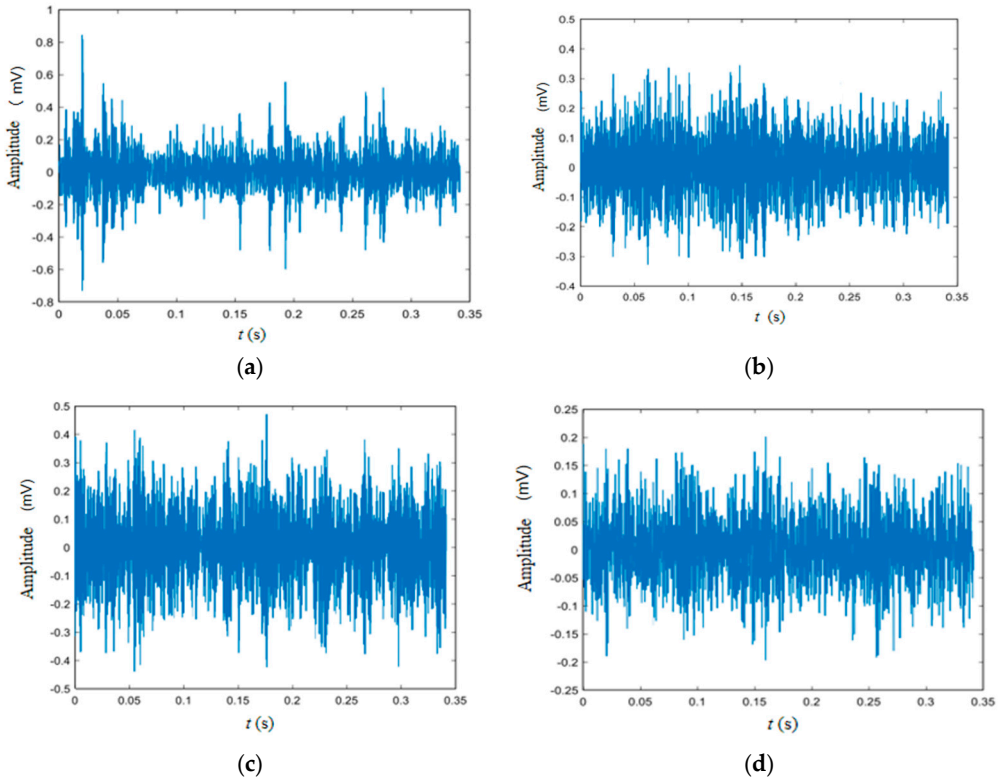


Figure 16. Time-domain Waveform After Separation: (**a**) Rolling element fault, (**b**) Cage fault, (**c**) Inner race fault, (**d**) Outer race fault.

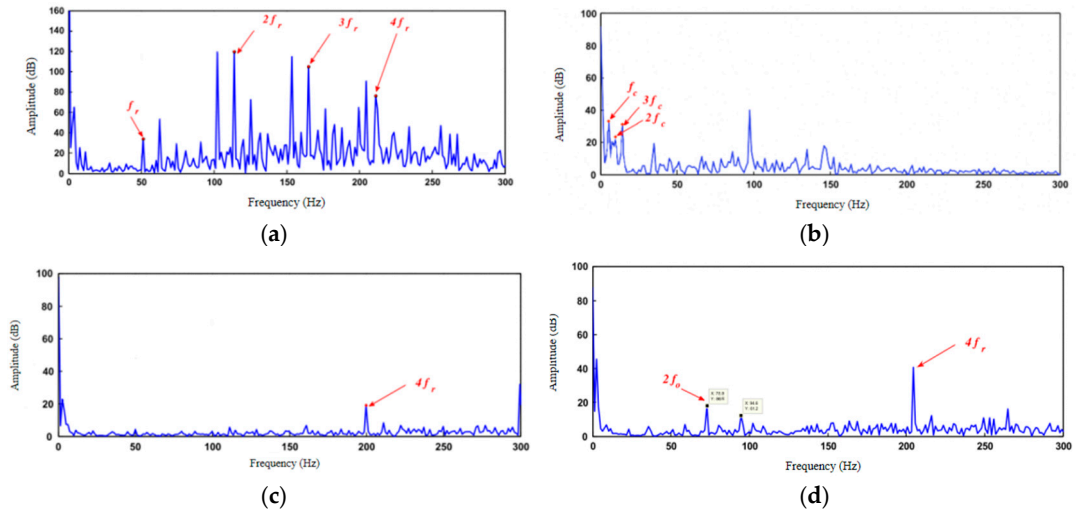


Figure 17. Spectral Features After Acoustic Signal Separation: (**a**) Rolling element fault, (**b**) Cage fault, (**c**) Inner race fault, (**d**) Outer race fault.

By comparing the spectral features in Figures 15 and 17, it is evident that in the spectrum of the signals that have not been separated using the AFSA algorithm, the characteristic information is completely drowned out by noise, making it impossible to extract any useful information. From Figure 17a, it can be seen that after the signal is separated using the AFSA algorithm, four fault characteristic frequencies are captured in the rolling element fault bearing spectrum, which are f_r, $2f_r$, $3f_r$, and $4f_r$. The energy distribution is mainly concentrated in the frequency range of 102 Hz to 220 Hz, thus identifying it as a rolling element fault. In Figure 17b, three fault characteristic frequencies are captured, which are f_c, $2f_c$, and $3f_c$. The energy distribution is mainly concentrated between 5.2 Hz

and 11.8 Hz, which expresses the characteristics of a cage fault. Surprisingly, Figure 17c only captures one frequency, $4f_r$, and does not capture the characteristic frequencies of the inner race fault. In Figure 17d, peaks at $2f_o$ and $4f_r$ appear, but no fault information is shown, even though the bearing used indeed has inner and outer race defects.

It is noteworthy that Figure 17a,c,d all coincidentally display the fault characteristic frequency $4f_r$ and sideband components with relatively high energy, suggesting that the bearing roller may have structural or machining defects.

We then input the source signal separated by the AFSA algorithm into the CEEMD denoising algorithm for noise reduction. The modal components are shown in Figure 18, and the correlation coefficients are listed in Table 7. Components with correlation coefficients greater than 0.1 were selected for signal reconstruction. Based on the processed results, the spectral features shown in Figure 18 are obtained.

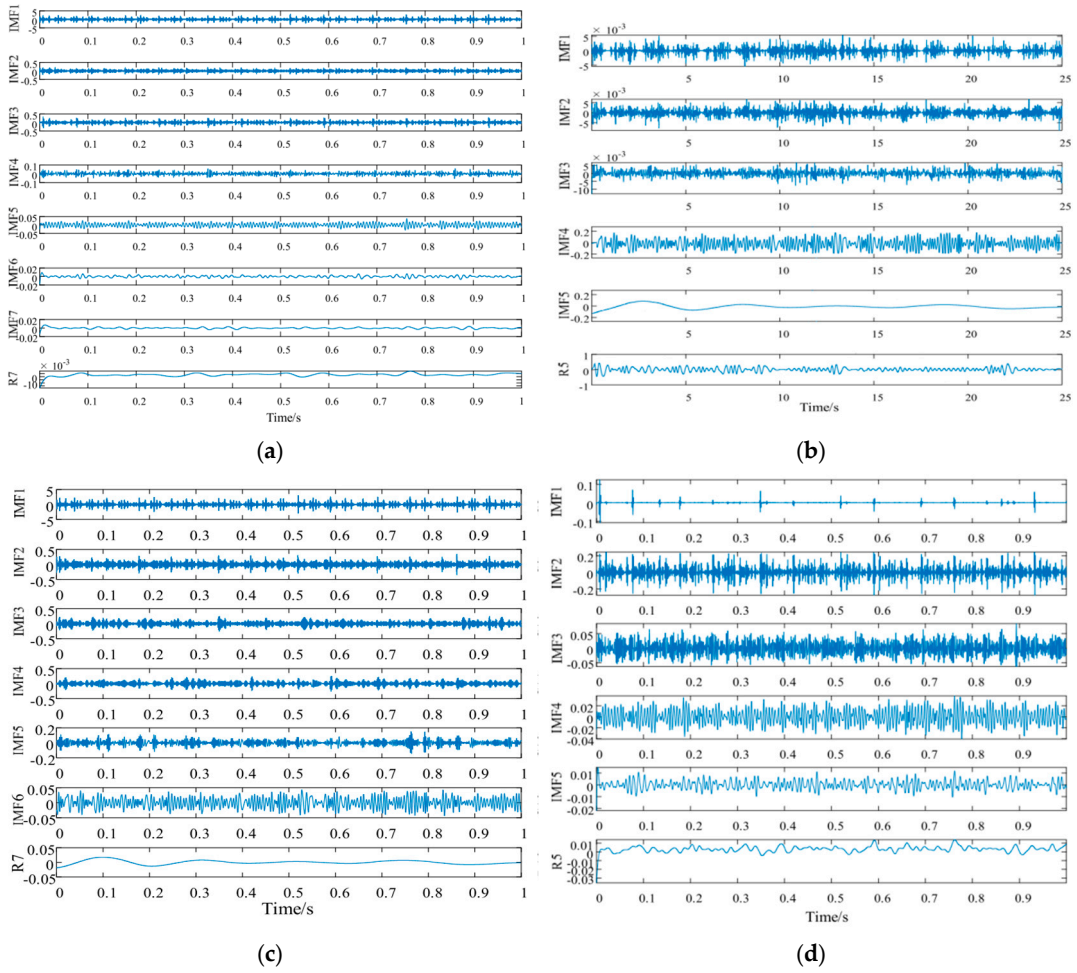


Figure 18. IMF Components: (**a**) Rolling element fault, (**b**) Cage fault, (**c**) Inner race fault, (**d**) Outer race fault.

Table 7. Correlation Coefficients.

	IMF1	IMF2	IMF3	IMF4	IMF5	IMF6	IMF7
Rolling element	0.96	0.21	0.15	0.16	0.17	0	0
Cage	0.97	0.19	0.14	0.11	0	0	0
Inner race	0.98	0.16	0.18	0.12	0.07	0	0
Outer race	0.08	0.33	0.17	0.10	0.02	0	0

After CEEMD denoising, the time-domain waveform is shown in Figure 19. By comparing Figure 20a with Figure 15a, it can be observed that during the operation of this rolling element bearing, the noise generated has affected the amplitude of the source signal [50] and also revealed the harmonics associated with the characteristic frequencies. As a result, the fault information is more distinct compared to the signal before denoising. From the comparison between Figures 15b and 20b, it is evident that, compared to the signal before denoising, the true amplitude of the fault characteristic frequencies is higher, with the $2f_c$ frequency being more prominent than before.

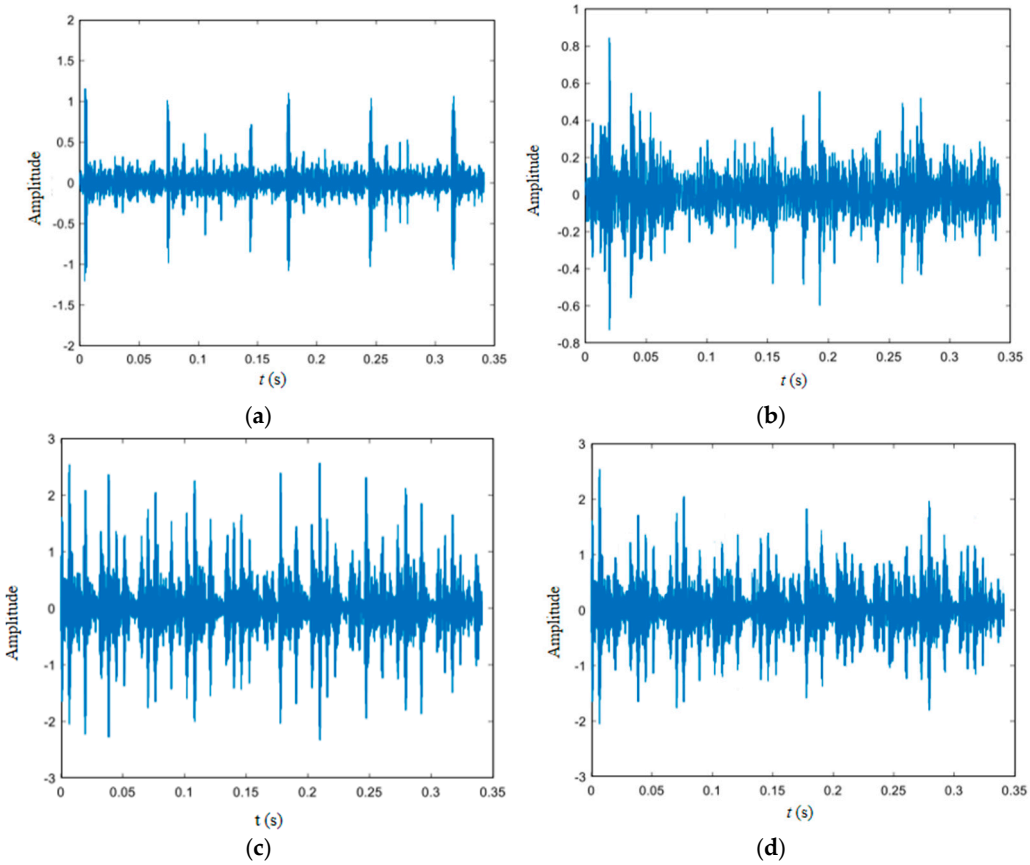


Figure 19. Time-domain Waveform After Denoising: (**a**) Rolling element fault, (**b**) Cage fault, (**c**) Inner race fault, (**d**) Outer race fault.

In Figure 20c, compared to Figure 15c, it can be seen that during the operation of this bearing, a significant amount of noise was generated, which caused the spectral features to be overwhelmed. However, three fault characteristic frequencies were successfully captured in Figure 20c, namely, $1f_i$, $2f_i$, and $3f_i$. The energy distribution of these frequencies is mainly concentrated in the range of 78.9 Hz to 228.7 Hz, representing the characteristics of an inner race fault.

In comparison with Figures 15d and 20d, it shows that, after denoising, we successfully captured the fault characteristic frequencies $1f_o$, $2f_o$, and $3f_o$, along with their sideband components. These spectral features correspond to an outer race fault. The sideband components generated in the above spectra [51] are preliminarily judged to be caused by impacts between the fault location and nearby components, resulting in modulated frequency bands where the modulation frequency corresponds to the rotational frequency and its harmonics.

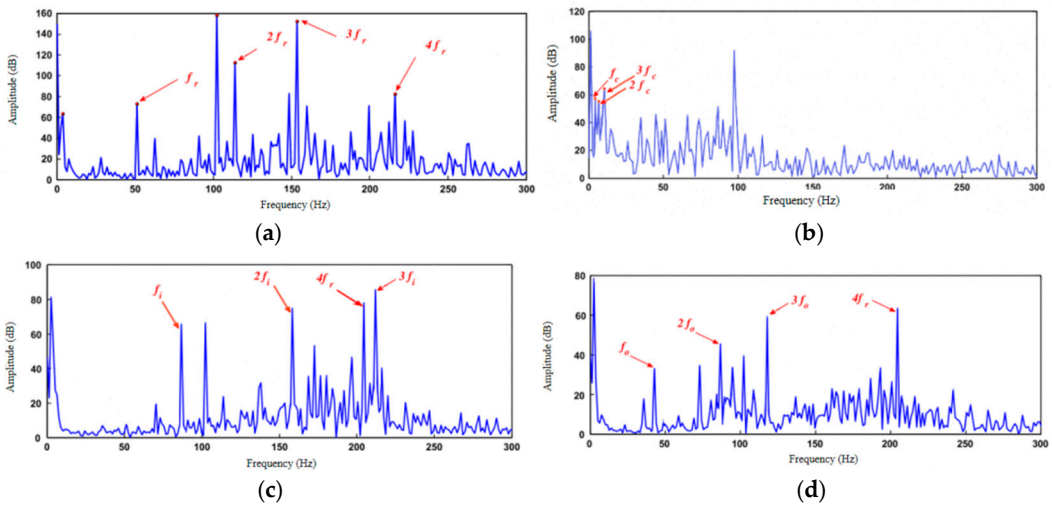


Figure 20. Spectral Features After CEEMD Denoising: (**a**) Rolling element fault, (**b**) Cage fault, (**c**) Inner race fault, (**d**) Outer race fault.

6. Discussion

6.1. In the Signal Separation Comparison Experiment

6.1.1. Signal Without AFSA Algorithm Separation (Figure 15)

(1) Spectral Characteristics: In the spectrum of the signal that has not been separated using the AFSA algorithm (Figure 15), the characteristic information is completely drowned out by noise, making it impossible to extract any useful information. This indicates that the original signal is heavily contaminated by noise, which makes it difficult to distinguish the fault characteristic frequencies.

(2) Analysis: This situation suggests that in the unoptimized signal, noise and fault information are mixed together, and traditional spectral analysis methods cannot effectively extract the fault characteristics.

6.1.2. Signal Separated Using the AFSA Algorithm

(1) Figure 17a: After separation using the AFSA algorithm, the spectrum of the bearing with rolling element fault captures four fault characteristic frequencies: f_r, $2f_r$, $3f_r$ and $4f_r$ and the energy of these characteristic frequencies is primarily concentrated in the frequency band of 102 Hz to 220 Hz, indicating that the rolling element fault has been effectively separated.

(2) Figure 17b: In this figure, after AFSA separation, three fault characteristic frequencies are captured: f_c, $2f_c$, and $3f_c$, with the energy distribution mainly concentrated between 5.2 Hz and 11.8 Hz, reflecting the characteristics of a cage fault.

(3) Figure 17c: In this figure, only one frequency $4f_r$ is captured, with no indication of the characteristic frequency for an inner race fault. This suggests that either the bearing may not have a significant inner race fault, or the separation algorithm has not fully captured the relevant features.

(4) Figure 17d: This figure shows peaks at frequencies $2f_o$ and $4f_r$, but there is no obvious fault information, possibly because the signal does not contain clear fault characteristics, or the noise is still affecting the separation effectiveness.

6.1.3. Statistical Analysis of Separation Similarity

(1) Spectral Feature Comparison: By comparing the spectra in Figures 15 and 17, it is clear that the spectrum of the signal separated using the AFSA algorithm can capture

the fault characteristic frequencies more clearly, and the impact of noise is significantly reduced. This demonstrates the effectiveness of the AFSA algorithm in signal separation.

(2) Statistical Analysis:

Signal Separation Effect: Figure 17a,b show that the energy is concentrated in specific frequency bands, and these bands correspond to the fault characteristic frequencies, indicating that the AFSA algorithm has effectively separated the fault information.

Noise Suppression: In the signals separated by the AFSA algorithm, the influence of noise is visibly reduced, and the spectrum is clearer, indicating that the algorithm performs excellently in noise suppression.

Through statistical analysis, the superiority of the AFSA algorithm in signal separation can be demonstrated. By comparing the spectrum of the separated signal with the unseparated signal, it is evident that the AFSA algorithm effectively extracts the fault characteristic frequencies, especially in Figure 17a,b, where the spectral features of rolling element and cage faults are distinctly identified. Moreover, the AFSA algorithm also shows advantages in noise suppression and energy concentration. However, the denoising effect is still not sufficient. Therefore, the following discussion will address the effects of applying the CEEMD denoising algorithm to the source signals separated by the AFSA algorithm.

6.2. Comparison Experiment Before and After CEEMD Denoising

6.2.1. Signal-to-Noise Ratio (SNR) Improvement

By comparing the SNR of the signal before denoising (as shown in Figure 15) and after denoising (as shown in Figure 19), and calculating the difference in SNR between the denoised signal in Figure 19 and the un-denoised signal in Figure 15a, a quantitative measure of the denoising effect is obtained. The SNR of the denoised signal is higher than that of the signal before denoising, indicating that the impact of noise on the signal has been reduced, and the signal is clearer.

6.2.2. Mean Squared Error (MSE) Reduction

By comparing the signal in Figure 15 and the denoised signal in Figure 20b, the MSE is calculated. The MSE value of the denoised signal is lower, indicating that after CEEMD denoising, the difference between the signal and the original (noise-free) signal has been reduced, and the signal has been more accurately restored.

6.2.3. Changes in Spectral Features

After denoising, the fault characteristic frequencies and harmonics are displayed more clearly. In Figure 20a, compared to Figure 15a, the denoised signal more clearly shows the fault characteristic frequencies, and the harmonic components are more prominent, suggesting a reduction in noise interference and a clearer representation of the signal's features. The spectrum in Figure 20b, compared with Figure 15b, shows an increase in the real amplitude of the fault characteristic frequencies, particularly the enhancement of the 2f frequency, indicating that the denoising process improved the recognizability of the signal and the extraction of fault information.

6.2.4. Quantitative Analysis Results

(1) Signal-to-Noise Ratio (SNR) Improvement: By comparing the SNR before and after denoising, it is quantitatively demonstrated that the denoising process effectively improves the signal quality and reduces noise interference.

(2) Mean Squared Error (MSE) Reduction: After denoising, the reduced MSE indicates that the difference between the denoised signal and the original noise-free signal is smaller, showing the effectiveness of the denoising process.

(3) Clearer Spectral Features: The denoised spectrum reveals richer and clearer fault characteristic frequencies, suggesting that the CEEMD denoising method effectively improves the signal's analyzability.

7. Conclusions

To address the limitations of directly applying aliased acoustic signals in rolling bearing fault diagnosis, this study proposes a composite denoising framework integrating various advanced signal processing techniques—namely, the Artificial Fish Swarm Algorithm (AFSA)-based acoustic signal separation, Fast Independent Component Analysis (FastICA), and Complementary Ensemble Empirical Mode Decomposition (CEEMD) for joint denoising in rolling bearing fault diagnosis.

Specifically, this study first uses the Artificial Fish Swarm Algorithm (AFSA) to deeply optimize FastICA, enabling precise global optimization of the mixing matrix. This optimization is followed by an inverse transformation of the mixing matrix to obtain a preliminary estimate of the source signals. As demonstrated in the aforementioned AFSA-FastICA simulation experiment, although the AFSA experienced slight fluctuations near the convergence value, the number of iterations with such fluctuations was minimal, thanks to the fish swarm algorithm's ability to assess the crowding degree, indicating that the algorithm did not become trapped in local optima for long periods. In contrast, FastICA showed fluctuations at different positions, suggesting that it is prone to falling into local optima, which also resulted in slower convergence, taking about 44 iterations to converge.

On this basis, the study further applies the Complementary Ensemble Empirical Mode Decomposition (CEEMD) algorithm to denoise the estimated source signals, using the cross-correlation coefficient as a selection criterion to effectively eliminate irrelevant modal components and accurately reconstruct the signal. As shown in the CEEMD denoising simulation experiment, comparing the completeness and orthogonality of EMD, EEMD, and CEEMD, it is evident that CEEMD has the best orthogonality and superior completeness compared to EMD and EEMD, resulting in the least modal mixing.

In the next step, detailed frequency-domain feature extraction is performed on the reconstructed signal using Fast Fourier Transform (FFT) to support precise rolling bearing fault diagnosis. Experimental data show that the AFSA-FastICA-CEEMD composite algorithm not only efficiently separates the target acoustic signal but also significantly suppresses noise components, ensuring high accuracy and reliability in rolling bearing fault diagnosis. As illustrated in the final results, the fault location is preliminarily identified as an impact between the faulty part and nearby components, with modulated frequency bands on the spectrum at the rotational frequency and its harmonics. From the final analysis of the experimental results, it can be concluded that by comparing the spectra of Figures 15c and 20c, it is clearly observed that in Figure 20c, three distinct fault characteristic frequencies, labeled as $1f_i$, $2f_i$, and $3f_i$, are successfully identified and captured. The energy of these frequencies is primarily distributed within the 78.9 Hz to 228.7 Hz range, with the spectral characteristics indicating a clear inner race fault. Further analysis of the spectra in Figures 20d and 15d reveals that, after noise suppression processing, the source signal spectrum successfully captures three additional key fault characteristic frequencies, $1f_o$, $2f_o$, and $3f_o$, along with their corresponding sideband components. These features are fully represented in the spectrum, confirming that the fault is closely associated with the outer race fault. This comprehensive signal processing strategy provides a more sophisticated and refined solution for rolling bearing fault diagnosis.

Author Contributions: Conceptualization, J.Y. and D.Z.; methodology, J.Y. and D.Z.; software, D.Z.; validation, D.Z. and F.Z.; formal analysis, F.Z. and D.Z.; investigation, F.Z. and X.Z.; resources, J.Y.; data curation, X.Z.; writing—original draft preparation, F.Z.; writing—review and editing, D.Z.;

visualization, J.Y.; supervision, J.Y.; funding acquisition, J.Y. All authors have read and agreed to the published version of the manuscript.

Funding: The authors gratefully acknowledge the support provided for this research by the Natural Science Foundation of Guangdong Province (2022A1515011562) and National Natural Science Foundation of China (52201355), by Guangdong Provincial Special Fund for promoting high quality economic development (Yuerong Office Letter [2020]161, GDNRC [2021]56), and Development of intelligent early warning system for regional equipment failure (CY-ZJ-19-ZC-005).

Data Availability Statement: The Case Western Reserve University dataset used in this paper is available at: https://gitcode.com/open-source-toolkit/78d4f/overview?utm_source=tools_gitcode&index=top&type=card&&isLogin=1 (accessed on 6 October 2024).

Acknowledgments: We acknowledge the support given by Guangdong Ocean University.

Conflicts of Interest: The authors declare no conflicts of interest.

References

1. Nandi, S.; Toliyat, H.A.; Li, X. Condition monitoring and fault diagnosis of electrical motors—A review. *IEEE Trans. Energy Convers.* **2005**, *20*, 719–729. [CrossRef]
2. Wang, X.; Zhao, J.; Wu, X. Comprehensive Separation Algorithm for Single-Channel Signals Based on Symplectic Geometry Mode Decomposition. *Sensors* **2024**, *24*, 462. [CrossRef] [PubMed]
3. Li, J.; Meng, Z.; Yin, N.; Pan, Z.; Cao, L.; Fan, F. Multi-source feature extraction of rolling bearing compression measurement signal based on independent component analysis. *Measurement* **2021**, *172*, 108908. [CrossRef]
4. Ding, H.; Wang, Y.; Yang, Z.; Pfeiffer, O. Nonlinear blind source separation and fault feature extraction method for mining machine diagnosis. *Appl. Sci.* **2019**, *9*, 1852. [CrossRef]
5. Wang, M.; Cui, X.; Wang, T.; Jiang, T.; Gao, F.; Cao, J. Eye blink artifact detection based on multi-dimensional EEG feature fusion and optimization. *Biomed. Signal Process. Control.* **2023**, *83*, 104657. [CrossRef]
6. Wang, Q.; Wang, L.; Yu, H.; Wang, D.; Nandi, A.K. Utilizing SVD and VMD for denoising non-stationary signals of roller bearings. *Sensors* **2022**, *22*, 195. [CrossRef]
7. Zhang, S.B.; Lu, S.L.; He, Q.B.; Kong, F. Time-varying singular value decomposition for periodic transient identification in bearing fault diagnosis. *J. Sound Vib.* **2016**, *379*, 213–231. [CrossRef]
8. Zhang, Q.C.; Liu, Y.S.; Yang, W. Underwater Transient Noise Duration Estimation Method Based on the Page Test. In Proceedings of the 2024 OES China Ocean Acoustics (COA), Harbin, China, 29–31 May 2024; IEEE: Piscataway, NJ, USA, 2024; pp. 1–4.
9. Das, S.; Khatri, S.; Saha, A. Position sensitive detector based non-contact vibration measurement with laser triangulation method utilizing Gabor Transform for noise reduction. *J. Vib. Control.* **2024**, *30*, 1984–1994. [CrossRef]
10. Mao, B.; Yang, H.; Li, W.; Zhu, X.; Zheng, Y. Multi-Frequency Noise Reduction Method for Underwater Radiated Noise of Autonomous Underwater Vehicles. *J. Mar. Sci. Eng.* **2024**, *12*, 705. [CrossRef]
11. Nguyen, C.D.; Kim, C.H.; Kim, J.M. Gearbox Fault Identification Model Using an Adaptive Noise Canceling Technique, Heterogeneous Feature Extraction, and Distance Ratio Principal Component Analysis. *Sensors* **2022**, *22*, 4091. [CrossRef]
12. Saber, T.; Achour, V.; Noura, A. Denoising sensors signals within mechatronic systems using EMD method. In Proceedings of the 2015 World Congress on Information Technology and Computer Applications (WCITCA), Hammamet, Tunisia, 11–13 June 2015.
13. Ren, G.; Liu, Z. An improved EMD adaptive denoising and feature extraction algorithm. In Proceedings of the 2019 IEEE International Conference on Signal Processing, Communications and Computing (ICSPCC), Dalian, China, 20–22 September 2019.
14. Wu, Z.; Huang, N.E. Ensemble empirical mode decomposition: A noise-assisted data analysis method. *Adv. Adapt. Data Anal.* **2009**, *1*, 1–41. [CrossRef]
15. Jin, T.; Li, Q.; Mohamed, M.A. A novel adaptive EEMD method for switchgear partial discharge signal denoising. *IEEE Access* **2019**, *7*, 58139–58147. [CrossRef]
16. Salunkhe, V.G.; Khot, S.M.; Desavale, R.G.; Yelve, N.P. Unbalance Bearing Fault Identification Using Highly Accurate Hilbert–Huang Transform Approach. *J. Nondestruct. Eval. Diagn. Progn. Eng. Syst.* **2023**, *6*, 031005. [CrossRef]
17. Neshat, M.; Adeli, A.; Sepidnam, G.; Sargolzaei, M.; Toosi, A.N. A review of artificial fish swarm optimization methods and applications. *Int. J. Smart Sens. Intell. Syst.* **2012**, *5*, 108. [CrossRef]
18. Pourpanah FWang, R.; Lim, C.P.; Wang, X.Z.; Yazdani, D. A review of artificial fish swarm algorithms: Recent advances and applications. *Artif. Intell. Rev.* **2023**, *56*, 1867–1903. [CrossRef]
19. Neshat, M.; Sepidnam, G.; Sargolzaei, M.; Toosi, A.N. Artificial fish swarm algorithm: A survey of the state-of-the-art, hybridization, combinatorial and indicative applications. *Artif. Intell. Rev.* **2014**, *42*, 965–997. [CrossRef]

20. Luan, X.Y.; Li, Z.P.; Liu, T.Z. A novel attribute reduction algorithm based on rough set and improved artificial fish swarm algorithm. *Neurocomputing* **2016**, *174*, 522–529. [CrossRef]
21. Lee, T.W. *Independent Component Analysis*; Springer: Boston, MA, USA, 1998.
22. Ablin, P.; Cardoso, J.F.; Gramfort, A. Faster independent component analysis by preconditioning with Hessian approximations. *IEEE Trans. Signal Process.* **2018**, *66*, 4040–4049. [CrossRef]
23. Langlois, D.; Chartier, S.; Gosselin, D. An introduction to independent component analysis: InfoMax and FastICA algorithms. *Tutor. Quant. Methods Psychol.* **2010**, *6*, 31–38. [CrossRef]
24. Miao, F.; Zhao, R.; Jia, L.; Wang, X. Multisource fault signal separation of rotating machinery based on wavelet packet and fast independent component analysis. *Int. J. Rotating Mach.* **2021**, *2021*, 9914724. [CrossRef]
25. Tharwat, A. Independent component analysis: An introduction. *Appl. Comput. Inform.* **2021**, *17*, 222–249. [CrossRef]
26. Erdogmus, D.; Hild, K.E.; Rao, Y.N.; Príncipe, J.C. Minimax mutual information approach for independent component analysis. *Neural Comput.* **2004**, *16*, 1235–1252. [CrossRef] [PubMed]
27. Barhatte, A.S.; Ghongade, R.; Tekale, S.V. Noise analysis of ECG signal using fast ICA. In Proceedings of the 2016 Conference on Advances in Signal Processing (CASP), Pune, India, 9–11 June 2016; IEEE: Piscataway, NJ, USA, 2016; pp. 118–122.
28. Hyvarinen, A. Fast and robust fixed-point algorithms for independent component analysis. *IEEE Trans. Neural Netw.* **1999**, *10*, 626–634. [CrossRef]
29. Zhang, Z.; Tang, X.; Liu, C.; Li, X.; Ren, S. Multiple ultrasonic partial discharge DOA estimation performance of KPCA Pseudo-Whitening mnc-FastICA. *Measurement* **2024**, *231*, 114596. [CrossRef]
30. Ce, J.; Yang, Y.; Peng, Y. A new FastICA algorithm of Newton's iteration. In Proceedings of the 2010 2nd International Conference on Education Technology and Computer, Shanghai, China, 22–24 June 2010; IEEE: Piscataway, NJ, USA, 2010; Volume 3, pp. V3-481–V3-484.
31. Sonfack, G.B.; Ravier, P. Application of Single Channel Blind Source Separation Based-EEMD-PCA and Improved FastICA algorithm on Non-intrusive Appliances Load identification. *J. Electr. Electron. Eng.* **2022**, *10*, 114–120.
32. Gu, J.; Peng, Y. An improved complementary ensemble empirical mode decomposition method and its application in rolling bearing fault diagnosis. *Digit. Signal Process.* **2021**, *113*, 103050. [CrossRef]
33. Huang, S.; Wang, X.; Li, C.; Kang, C. Data decomposition method combining permutation entropy and spectral substitution with ensemble empirical mode decomposition. *Measurement* **2019**, *139*, 438–453. [CrossRef]
34. Pan, Z.; Xu, B.; Chen, W.; Fan, D.; Meng, X.; Peng, M.; Zhou, C. Improved Complete Ensemble Empirical Mode Decomposition with Adaptive Noise and Its Application in Noise Reduction for Fiber Optic Sensing. *J. Light. Technol.* **2024**, *43*, 2466–2474. [CrossRef]
35. Yeh, J.R.; Shieh, J.S.; Huang, N.E. Complementary ensemble empirical mode decomposition: A novel noise enhanced data analysis method. *Adv. Adapt. Data Anal.* **2010**, *2*, 135–156. [CrossRef]
36. Huang, N.E.; Shen, Z.; Long, S.R.; Wu, M.C.; Shih, H.H.; Zheng, Q.; Yen, N.-C.; Tung, C.C.; Liu, H.H. The empirical mode decomposition and the Hilbert spectrum for nonlinear and non-stationary time series analysis. *Proc. R. Soc. Lond. Ser. A Math. Phys. Eng. Sci.* **1998**, *454*, 903–995. [CrossRef]
37. Zheng, H.; Dang, C.; Gu, S.; Peng, D.; Chen, K. A quantified self-adaptive filtering method: Effective IMFs selection based on CEEMD. *Meas. Sci. Technol.* **2018**, *29*, 085701. [CrossRef]
38. Wang, M.; Bai, L.; Luo, L.; Jin, Y.; He, R.; Guo, S. An underdetermined environmental sound source separation algorithm based on improved complete ensemble EMD with adaptive noise and ICA. In Proceedings of the 2021 IEEE 21st International Conference on Communication Technology (ICCT), Tianjin, China, 13–16 October 2021; IEEE: Piscataway, NJ, USA, 2021; pp. 1335–1340.
39. Sun, H.; Wang, H.; Guo, J. A single-channel blind source separation technique based on AMGMF and AFEEMD for the rotor system. *IEEE Access* **2018**, *6*, 50882–50890. [CrossRef]
40. Yang, J.; Wang, X.; Wu, J.; Fen, Z. A noise reduction method based on CEEMD-RobustICA and its application in pipeline blockage signal. *J. Appl. Sci. Eng.* **2019**, *22*, 1–10.
41. Tao, R.; Zhang, Y.; Wang, L.; Zhao, X. Research of tool state recognition based on CEEMD-WPT. In Proceedings of the Cloud Computing and Security: 4th International Conference, ICCCS 2018, Haikou, China, 8–10 June 2018; Revised Selected Papers, Part II 4. Springer International Publishing: Cham, Switzerland, 2018; pp. 59–70.
42. Jiang, H.M.; Xie, K.; Wang, Y.F. Optimization of pump parameters for gain flattened Raman fiber amplifiers based on artificial fish school algorithm. *Opt. Commun.* **2011**, *284*, 5480–5483. [CrossRef]
43. Bo, X.; Fengxing, Z.; Kang, Y.B.; Huipeng, L.; Yi, L.; Dan, Y. Least squares mutual information for grid search CEEMD: A suitable vibration signal analysis method. In Proceedings of the 2018 37th Chinese Control Conference (CCC), Wuhan, China, 25–27 July 2018; IEEE: Piscataway, NJ, USA, 2018; pp. 5741–5748.
44. Hou, S.; Guo, W. Faulty Line Selection Based on Modified CEEMDAN Optimal Denoising Smooth Model and Duffing Oscillator for Un-Effectively Grounded System. *Math. Probl. Eng.* **2020**, *2020*, 5761642. [CrossRef]

45. Hou, S.; Guo, W. Optimal denoising and feature extraction methods using modified CEEMD combined with duffing system and their applications in fault line selection of non-solid-earthed network. *Symmetry* **2020**, *12*, 536. [CrossRef]
46. Zhang, F.; Gao, S.; Zhang, W.; Li, G. Improved EEMD and overlapping group sparse second-order total variation. *J. Braz. Soc. Mech. Sci. Eng.* **2024**, *46*, 386. [CrossRef]
47. Lu, Y.; Xie, R.; Liang, S.Y. CEEMD-assisted bearing degradation assessment using tight clustering. *Int. J. Adv. Manuf. Technol.* **2019**, *104*, 1259–1267. [CrossRef]
48. Zhong, T.; Qin, C.J.; Shi, G.; Zhang, Z.; Tao, J.; Liu, C. A residual denoising and multiscale attention-based weighted domain adaptation network for tunnel boring machine main bearing fault diagnosis. *Sci. China Technol. Sci.* **2024**, *67*, 2594–2618. [CrossRef]
49. Lv, Y.; Zhao, W.; Zhao, Z.; Li, W.; Ng, K.K. Vibration signal-based early fault prognosis: Status quo and applications. *Adv. Eng. Inform.* **2022**, *52*, 101609. [CrossRef]
50. Zuo, L.Q.; Sun, H.M.; Mao, Q.C.; Liu, X.Y.; Jia, R.S. Noise suppression method of microseismic signal based on complementary ensemble empirical mode decomposition and wavelet packet threshold. *IEEE Access* **2019**, *7*, 176504–176513. [CrossRef]
51. Kim, Y.; Ha, J.M.; Na, K.; Park, J.; Youn, B.D. Cepstrum-assisted empirical wavelet transform (CEWT)-based improved demodulation analysis for fault diagnostics of planetary gearboxes. *Measurement* **2021**, *183*, 109796. [CrossRef]

Disclaimer/Publisher's Note: The statements, opinions and data contained in all publications are solely those of the individual author(s) and contributor(s) and not of MDPI and/or the editor(s). MDPI and/or the editor(s) disclaim responsibility for any injury to people or property resulting from any ideas, methods, instructions or products referred to in the content.